Domain-engineered pyroelectric radiometer

John Lehman, George Eppeldauer, J. Andrew Aust, and Miklos Racz

We built a large-area domain-engineered pyroelectric radiometer with high spatial and spectral response uniformity that is an excellent primary transfer standard for measurements in the near- and the mid-infrared wavelength regions. The domain engineering consisted of inverting the spontaneous polarization over a 10-mm-diameter area in the center of a uniformly poled, 15.5 mm × 15.5 mm square, 0.25-mm-thick $LiNbO_3$ plate. Gold black was used as the optical absorber on the detector surface, and an aperture was added to define the optically sensitive detector area. Our results indicate that we significantly reduced the acoustic sensitivity without loss of optical sensitivity. The detector noise equivalent power was not exceptionally low but was nearly constant for different acoustic backgrounds. In addition, the detector's spatial-response uniformity variation was less than 0.1% across the 7.5-mm-diameter aperture, and reflectance measurements indicated that the gold-black coating was spectrally uniform within .2%, from 800 to 1800 nm. Other detailed evaluations of the detector include detector responsivity as a function of temperature, electrical frequency response, angular response, and field of view.

OCIS codes: 040.0040, 120.5630, 230.0230.

1. Introduction

Recently it was shown that techniques employed for domain engineering of lithium niobate ($LiNbO_3$) optical parametric oscillators could be used to create large-area, pyroelectric detectors that have reduced acoustic sensitivity.[1] On the basis of our earlier success, we incorporated a unique, concentric-ring patterned, domain-engineered pyroelectric detector into a complete radiometer. First, we discuss the domain-engineering aspects of our design. Then we describe the most important optical and electronic design considerations along with our measurement results.

2. Acoustic Nulling

Ferroelectric pyroelectric detectors are also piezoelectric; therefore the acoustic sensitivity is related to the mechanical structure of the detector, its environment, and anything to which it is attached. A strategy to reduce the pyroelectric detector acoustic sensitivity is shown schematically in Fig. 1. Two detector regions, (a) and (b), with equal and opposite acoustic sensitivities, are exposed to ambient conditions, whereas radiant power reaches only one detector region. The two detectors are connected electrically in parallel so that the current signal from one is superimposed on the other. The result may be expressed as

$$i = i_{a,\mathrm{pyro}} + i_{a,\mathrm{piezo}} + i_{b,\mathrm{piezo}}, \quad (1)$$

where i_{pyro} is the current generated from radiant-power input and i_{piezo} is the current generated from ambient acoustic noise surrounding the detector. If the piezoelectric current generated by detector (a) is equal to detector (b) (that is, if both detectors are mechanically identical), then simply,

$$i = i_{a,\mathrm{pyro}}. \quad (2)$$

In the present device, the center of the detector is effectively region (a) and region (b) is the outer ring. One electrode is placed on each face of the $LiNbO_3$ plate, and, consequently, the two detector regions are electrically connected in parallel. The outer ring is optically and acoustically sensitive, but an aperture prevents incoming optical radiation from being received.

In the past we observed 40-dB reduction in common mode signals over a range of frequencies and nearly 120 dB at what appear to be resonant frequen-

J. Lehman (lehman@boulder.nist.gov) and J. A. Aust are with the Optoelectronics Division, National Institute of Standards and Technology, Boulder, Colorado 80303. G. Eppeldauer is with the Optical Technology Division, National Institute of Standards and Technology, Gaithersburg, Maryland 20899-3460. M. Racz is a guest researcher at the National Institute of Standards and Technology from the Hungarian Academy of Sciences Research Institute for Technical Physics and Materials Science, Budapest, Hungary.

Received 23 June 1999; revised manuscript received 3 September 1999.

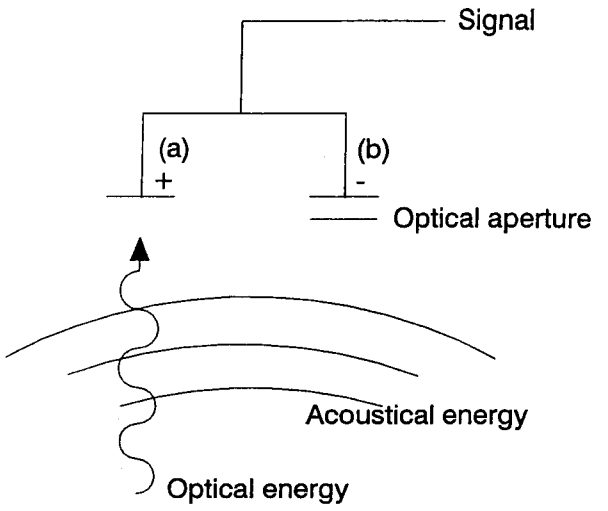

Fig. 1. Diagram of the acoustic nulling concept with equal and opposite pyroelectric domain areas.

cies in a bicell detector with bilateral symmetry. We chose a concentric-ring pattern to simplify the radiometer construction. In the future we expect to model different package geometries and domain patterns rather than rely on the process of trial and error to optimize the nulling capability of each detector.

In Section 4 (which deals with acoustic measurement) we compare two detectors. The steps for fabricating each detector are identical, with the exception of several intermediate steps taken in one of the detectors, to accomplish the selected-area electric field poling or the domain engineering. When we subsequently describe our measurements, the uniformly poled detector was designated J15 and the domain-engineered detector was designated J10. Detector J10 is then incorporated into the radiometer.

The pyroelectric detector elements were constructed from a commercially available, z-cut $LiNbO_3$ wafer. The wafer was 75 mm in diameter, 250 μm thick, and optically polished on both the positive and the negative z faces so that thickness variations were less than $\pm 0.25\%$ (manufacturer specification). The wafer was cut into 15.5 mm $\times$ 15.5 mm squares to form plates, which would eventually become the individual detector elements. To perform the domain reversal, the positive z face of the plate was coated with photoresist. A 10.8-mm-diameter opening was patterned in the center of the plate by use of standard photoresist processing. The sample was then clamped in an acrylic fixture with silicone O rings as shown in Fig. 2. Liquid electrodes were used to provide independent electrical contact to the positive and the negative z faces of the plate. The portion of the sample that underwent domain reversal was defined by the opening in the photoresist. Complete domain reversal of this area was achieved by application of a 24.5-kV/mm electric field across the electrodes.

The detector electrodes were fabricated by deposition of circular nickel films, 15.2 mm in diameter and 25 nm thick in the center of each z face of the plates. The final step in constructing the detector element was the deposition of the gold-black absorbing layer. The process by which the gold black is deposited is similar to that documented by others, most notably Blevin and Brown,[2] but is not substantially different from that documented by Harris *et al.* in 1948.[3] Our process depends on the product of the pressure of the nitrogen environment in which the gold is evaporated and on the distance from the filament source and the target (the nickel-coated $LiNbO_3$ plate). A rule of thumb is "10 Torr cm." In other words, the product of the distance between the evaporation source and the target should equal 12 Pa m (10 Torr cm). Depositing gold black on a thin, fragile, dielectric material, remains an art. The ability to conduct heat away from the crystal is crucial during the deposition, but a uniform and substantial heat sink (without contact resistance) is difficult to attach without scratching or breaking the $LiNbO_3$ plate. In this case we used gold foil sandwiched between the plate and a 3-mm-thick aluminum stage. The plate was held lightly with a spring retainer.

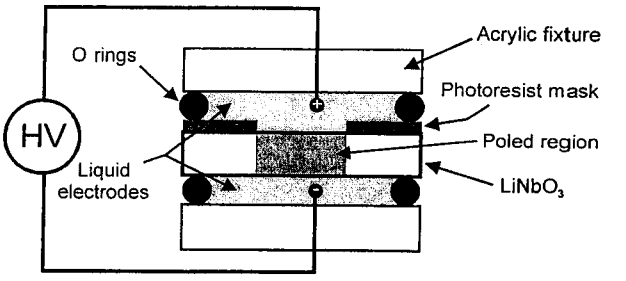

Fig. 2. Schematic diagram of the fixture for applying a high-voltage (HV) electric field across the $LiNbO_3$ plate.

A schematic view of the domain-engineered pyroelectric detector element is shown in Fig. 3. A cross-sectional view of the complete detector assembly is shown in Fig. 4. The detector element was attached electrically and mechanically to the container with electrically conducting epoxy on the perimeter of the aperture. As a result the signal electrode was not attached to a rigid heat sink and therefore provided a

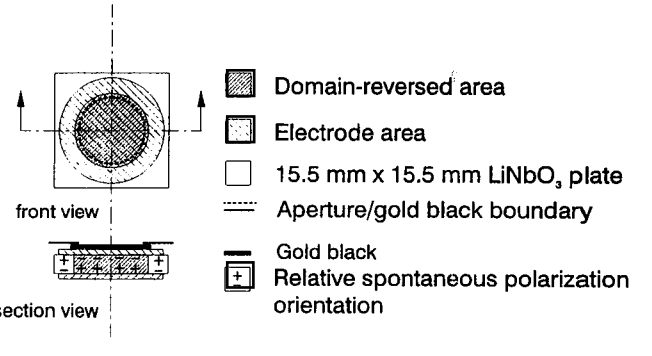

Fig. 3. Exploded view of spontaneous polarization, electrodes, aperture, and gold black.

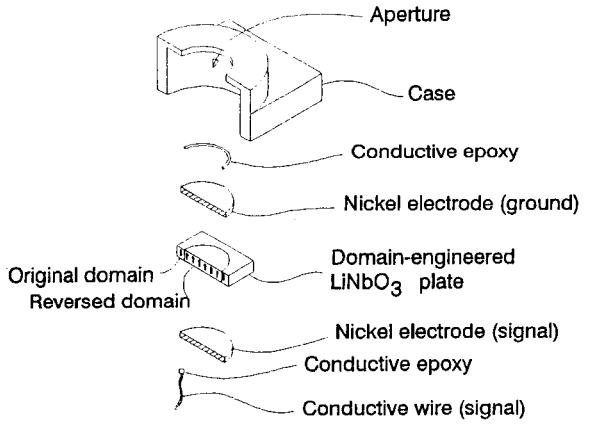

Fig. 4. Perspective-section view of $LiNbO_3$ packaging.

more spatially uniform response to optical input. The grounded case provided electromagnetic shielding for the signal electrode.

Because pyroelectric materials are also piezoelectric, the pyroelectric detector response may contain frequency components in the range of the optical chopping frequency. The typical detector figure of merit, noise-equivalent power (NEP), is normally specified (or should be) along with the wavelength, chopping frequency, bandwidth, detector area, and sometimes temperature and feedback resistance. NEP is a well-accepted, commonly used noise-sensitivity figure of merit for all types of optical detectors, but it is dubious for pyroelectric detectors, because it does not account for the acoustic background.

We compared the acoustic response of our domain-engineered detector, J10, which has equal and opposite areas of acoustic sensitivity, with an otherwise identical, uniformly poled detector, J15. We measured the relative acoustic frequency response by using a loudspeaker located 45 mm away from the detector aperture and facing it. The loudspeaker output was coupled to the pyroelectric detector through the surrounding air. The pyroelectric detector output was sampled and recorded over the frequency range of 5–100 Hz with a lock-in amplifier. The results are shown in Fig. 5. We were interested in low-frequency responsivity, because the minimum NEP typically is found at a frequency of less than 100 Hz.[4] Over the chopping frequency range of interest the responsivity of the domain-engineered detector was 7–15 dB less than that measured by the uniformly poled detector, for identical measurement conditions.

3. Radiometer Construction

The domain-engineered pyroelectric detector was placed in the radiometer assembly shown in Fig. 6. The detector and the connecting wires were mounted in an aluminum block. This block was attached to the aluminum, electrical-shield housing of the electronics. The output leads of the pyroelectric detector were connected to the current-to-voltage

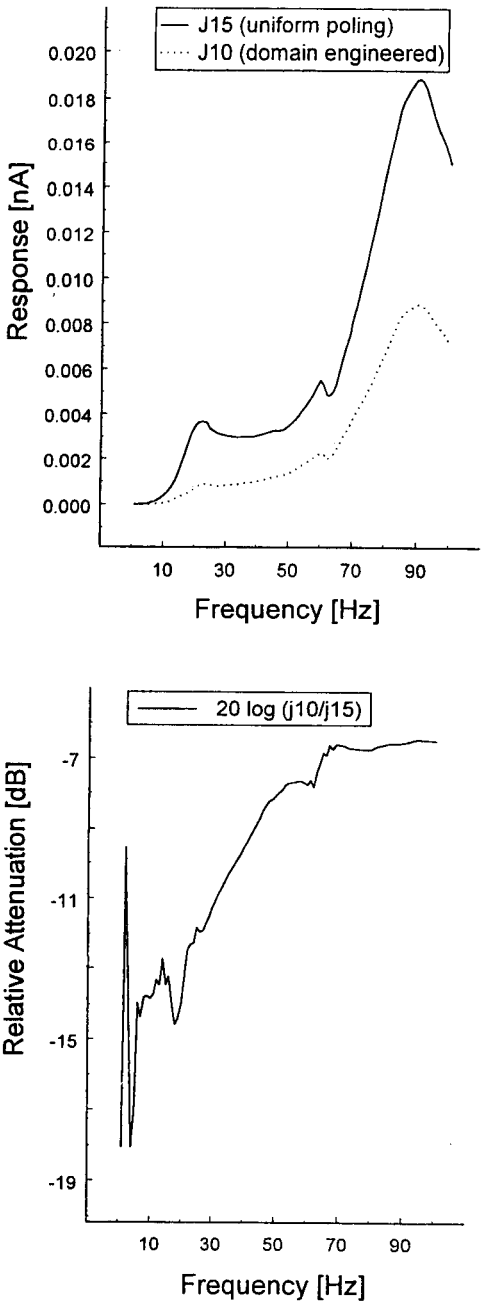

Fig. 5. Acoustic frequency response for two pyroelectric detectors that were identical except for the poling orientation (detector J15, uniform poling; detector J10, domain engineered).

converter input. To avoid 60-Hz pickup, the housing of the electronics and the detector block were continuously grounded. To avoid ground loops, the signal common and the shield were connected only at the 0-V output of the ±15-V power supply. A thermistor was mounted inside a copper plate with good thermal contact to the detector to monitor the detector temperature.[5]

We use a custom-made current-to-voltage converter (current preamplifier) along with a commercially available lock-in amplifier and chopper to obtain a usable signal from the pyroelectric detector.

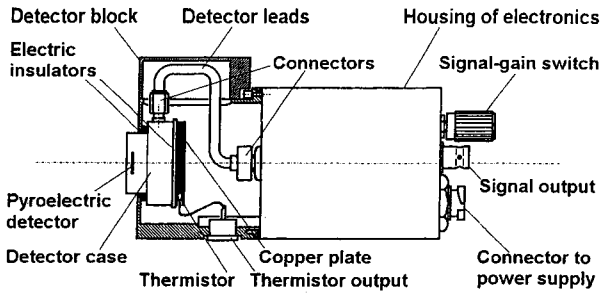

Fig. 6. Radiometer construction incorporating the domain-engineered pyroelectric, j10.

This is a common approach with pyroelectric detectors. However, there are many subtleties in designing and using the current-to-voltage converter to optimize the detector performance.

The equivalent circuit for any pyroelectric detector is modeled as a current generator along with a resistor and a capacitor, electrically connected in parallel. The current-to-voltage converter was used to measure the short-circuit current from the pyroelectric detector signal electrode. Connecting external capacitors, parallel to the feedback resistors of the converter, optimized the signal- and loop-gain requirements. The signal roll-off frequencies were tuned to a range between 100 and 1000 Hz. Optimization of the converter-voltage gain-versus-frequency curve was not necessary, because the dominant noise was the current noise of the pyroelectric detector. Consequently, selection of operational amplifiers for the converter was not a critical issue.

To avoid signal distortion, including amplitude decrease and signal phase shift, the signal shape of the output voltage must be similar to the shape of the chopped optical signal. To achieve this similarity, the fundamental gains of the photocurrent meter (including the detector and the converter) must be optimized at the signal frequencies.[6] The signal gains should be frequency independent (flat) around the signal (chopping) frequency to avoid signal-gain instabilities. To achieve this requirement, the 3-dB roll-off frequencies of the signal-gain characteristics were tuned 1 decade higher than the chopping frequency. Also, the chopping frequency was selected low. For the highest feedback resistor, the stray capacitance produced a relatively low signal roll-off frequency. It was necessary to carefully connect the feedback components of the converter to keep the stray capacitance low and the 3-dB roll-off signal frequency high. The 3-dB points should not be much more than 1 decade higher than the signal frequency, especially at low signal-gain ranges; otherwise the loop-gain at the chopping frequency can be too small, resulting in low-accuracy current-to-voltage conversion.

All of our electronic and radiometric tests were made with an ac data-acquisition system.[7] The voltage output of the pyroelectric radiometer was attached to the input of a dual-phase, sine-wave

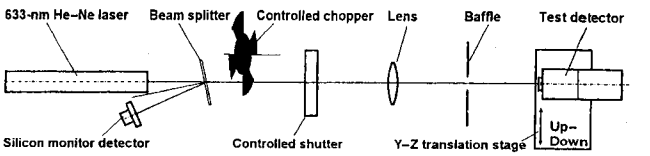

Fig. 7. Arrangement for frequency-response and spatial-response uniformity measurements.

measuring lock-in amplifier. The in-phase- and the quadrature-analog lock-in outputs were recorded by two simultaneously triggered digital voltmeters (DVM's) that served as analog-to-digital converters for the lock-in. These two DVM output channels (X and Y) are summed in quadrature digitally by the computer to extract the signal magnitude. Low-pass filtering of the analog signals is achieved by the integrating-time constants of the averaging times of both the lock-in outputs and the DVM's. In our measurements the lock-in output time constant was set to 333 ms. The DVM's were always operated with an averaging time of 100 power-line cycles.

4. Measurements

The frequency-dependent response of the radiometer was tested with the optical arrangement shown in Fig. 7. The primary beam from a He–Ne laser was chopped with a mechanical chopper and focused onto the pyroelectric detector with a plano–convex lens. The monitoring beam was reflected with a beam splitter and directed to underfill a silicon-monitor detector. The pyroelectric-detector signal was corrected with the monitor-detector signal to compensate for optical power fluctuations in the primary beam. A shutter and baffle minimized uncertainties due to stray radiation.

Figure 8 shows the gain-versus-frequency characteristics of the domain-engineered pyroelectric detector for the two highest signal-gain selections. Both curves were normalized to the zero-signal frequency. Two signal-gain ranges, 10^9 and 10^8 V/A, were the only ranges for which no external compensating capacitors were needed. The 3-dB roll-off point was 61

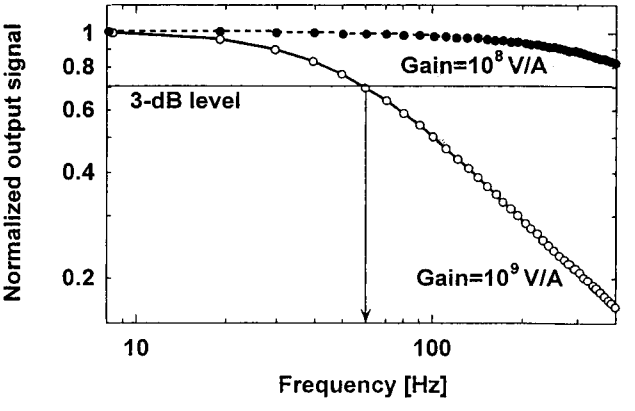

Fig. 8. Measured signal gain-versus-frequency curves of the domain-engineered pyroelectric radiometer.

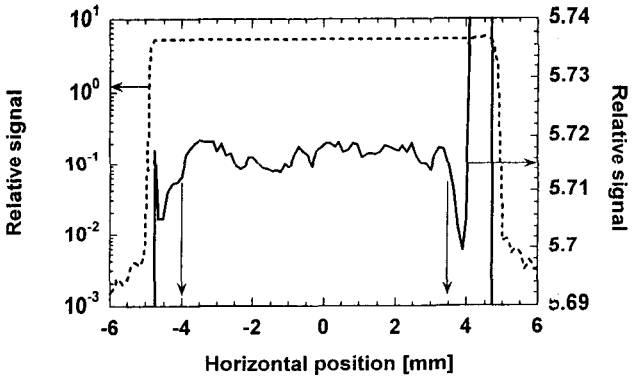

Fig. 9. Horizontal spatial-response scan of the pyroelectric radiometer.

Hz for the 10^9 V/A gain and 570 Hz for the 10^8 V/A gain. Figure 8 also shows that the signal-amplitude attenuation will be negligible even at the highest signal gain (10^9 V/A) if a sufficiently low chopping frequency is selected, in this case, 8–10 Hz.

The spatial-response uniformity of the pyroelectric detector was measured along two perpendicular axes across the center of the detector. The spot diameter of the probe beam on the detector was less than 0.5 mm. The horizontal- and the vertical-response scans are shown in Figs. 9 and 10. The graphs show that the spatial-response changes are 0.3% (maximum to minimum) across a properly positioned 7.5-mm-diameter aperture. With this aperture the standard deviation, calculated from the scanned points, was 0.03% for the horizontal and 0.09% for the vertical diameters. These uncertainties will be decreased if larger beam spots are used and positioned systematically at the center of the aperture. The response increase at the edges was caused by the reflected (converging) beam from the shiny housing around the detector.

The radiant-power response and the noise floor were measured with a mechanically chopped, 633-nm-wavelength laser beam for optical input. Neutral-density filters were used to attenuate the laser power at seven levels ranging from 624 μW to 1.7 nW. The chopper was positioned close to the

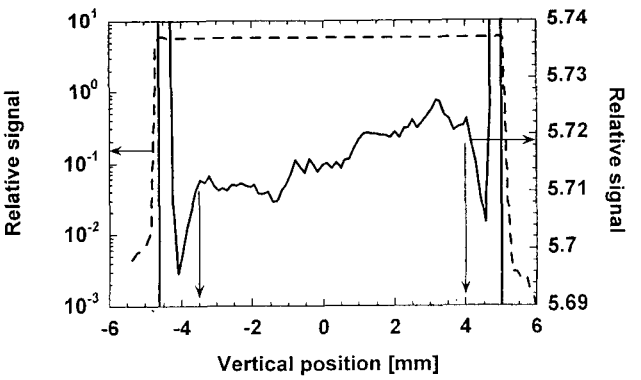

Fig. 10. Vertical spatial-response scan of the pyroelectric radiometer.

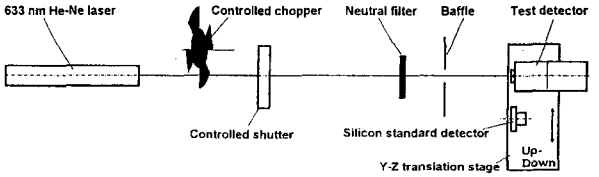

Fig. 11. Arrangement of the pyroelectric radiometer response and noise measurements.

laser to minimize detection of frequency-modulated stray radiation. Also, a baffle was located close to the detector to keep the field of view for the chopped radiation small. The reference for the power response and the response nonlinearity of the pyroelectric detector was a silicon photodiode with an area of 1 cm^2. During the test the pyroelectric detector position was alternated with the reference silicon photodiode position. The optical arrangement of the measurements is shown in Fig. 11.

The radiant-power response and the noise-floor measurements were used to calculate the detector's NEP at each radiant power. In nearly each case the power measurement was followed by a dark measurement. The difference between the power and the dark measurements was equal to the signal. The photocurrent-to-voltage gain for the pyroelectric detector preamplifier was 10^9 A/V, and the chopping frequency was 10 Hz. A pyroelectric detector response of 0.1045 μA/W was measured at 578-μW laser power.

For high signal-to-noise ratios the signal was calculated and averaged from approximately twenty samples. When the signal-to-noise ratio was low, the noise in the X and the Y channels was rectified, resulting in residual output offset. To avoid the output offset, the signal was calculated differently. Instead of subtracting a dark measurement result from the corresponding power measurement result, we made the averages separately for both the power and the dark values of the X and the Y channels. Thereafter, the difference of the average-dark measurement and the average-power measurement was calculated with the vectorial sum process.

We calculated the NEP values shown in Fig. 12

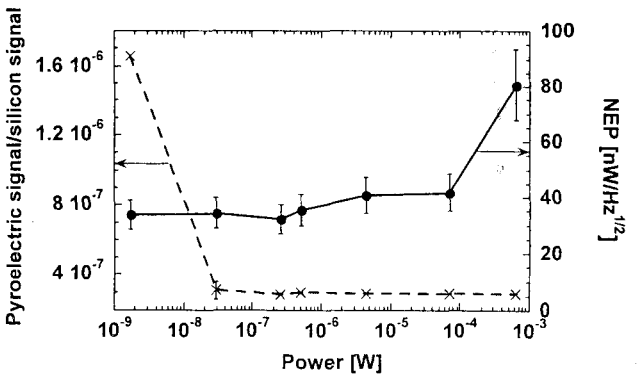

Fig. 12. Response linearity and NEP of the domain-engineered pyroelectric radiometer versus radiant power.

from the standard deviations of the power readings by evaluating the quadrature sum of the X and the Y output readings. The dark measurements were not used, to avoid the quadrature sum of the two noise readings.

Figure 12 shows that the NEP was flat from 1.7 nW to ~0.1 mW (solid curve) and is equal to ~38 nW/$Hz^{1/2}$. At high radiant power the measured NEP was twice the low-level NEP, probably because of additional noise sources, such as laser noise, in the measurement system. The relative uncertainty ($k = 1$) of the NEP determinations (calculated from 20 measurements) was 16%.[8] The results suggest that it is enough to measure NEP at one signal level, which can be in the dark. The typical dark NEP, measured separately (not shown in the figure), was 32 nW/$Hz^{1/2}$.

Figure 12 also shows the pyroelectric detector response linearity compared with a previously characterized silicon photodiode.[9] The ratio of the pyroelectric detector signal to the silicon detector signal (left-hand axis in Fig. 12) shows linear detector responsivity over 6 decades. The outlying point is caused by the poor signal-to-noise ratio of the pyroelectric detector at the low-power end. Here the uncertainty is 2.6 times larger than the measured ratio. This large error bar is not shown in the graph. The error bars (the uncertainties calculated from the relative standard uncertainties of the measured ratios) are shown for all the other ratios. At 29 nW the error bar can be seen well. At higher power the error bars are too small to be seen on the graph.

The ultimate check of our NEP measurements is practical and somewhat qualitative. Pyroelectric detectors are notoriously sensitive to ambient noise ranging from fan motors to slamming doors and other laboratory equipment. We measured the noise levels under various conditions. The radiometer was wrapped with insulation foam and situated in different locations on the detector stage when the servomotor (which moves the stage) was on and off. Identical tests were also performed without the insulation foam and in other locations in the lab. The NEP did not show any significant change during the tests. The NEP for other types of pyroelectric detectors varied by a factor of nearly 10, during similar tests.

In 1975 Byer described a complementary domain-engineered pyroelectric detector with reduced sensitivity to temperature changes. He also suggested that a domain-engineered detector with equally and oppositely poled areas within a single crystal should have a response completely independent of ambient temperature fluctuations. However, his results do not indicate that complete independence is achievable, nor do ours.[10] This is perhaps an area for future study, because $LiNbO_3$ (and $LiTaO_3$) pyroelectric detectors have a strong ambient temperature dependence, which is undesirable for highly accurate radiometers. For now, we are satisfied with slightly reduced temperature dependence in the domain-engineered pyroelectric detector and rely on correction factors, or active thermal stabilization, to ensure that the radiometer response is independent of ambient temperature fluctuations.

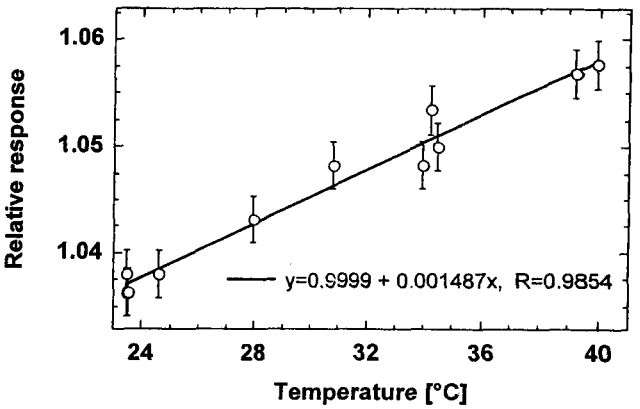

Fig. 13. Domain-engineered pyroelectric radiometer, relative response versus temperature.

The temperature-dependent response of the pyroelectric detector was tested to determine the response correction factors for a range of ambient temperatures. During the test the 633-nm laser beam, incident on the detector, was stabilized. An insulated-electric heater was attached to the outside surface of the detector package. The temperature was increased slowly from 23.5 to 40 °C. The signal and the temperature outputs were simultaneously recorded during both the heating and the cooling cycles at several different temperatures. The relative response-versus-temperature curve is shown in Fig. 13. A response temperature coefficient of 0.15%/°C was obtained from a linear fit to the measured data points. The error bars represent a 0.25% uncertainty (coverage factor, $k = 1$) for the measured values. From the data shown in Fig. 13, the relationship for the response of the pyroelectric detector at a calibration temperature T_c is R_c. The response at a different measurement temperature T_m will be

$$R_m = R_c f. \tag{3}$$

The response correction factor may be used where $f = 1 + (\Delta T \times C_T)$, $\Delta T = T_c - T_m$, and the response temperature coefficient is $C_T = 0.0015$.

Pyroelectric materials are inherently spectrally flat over a broad wavelength range.[11] Therefore the spectral responsivity of a pyroelectric detector is dependent on the reflectance of the face electrodes and other materials placed on the detector surface to efficiently convert optical energy into thermal energy. The advantages and disadvantages of commercially available optical coatings have been well documented.[12] Though easily damaged by the slightest touch, or excessive heat (greater than 200 mW/cm^2), gold black is our absorber of choice.

Published data show that gold-black coatings diffusely reflect less than 1% of incident radiation, over a spectral range from the ultraviolet to 15 μm.[13] We

have been unable reproduce these results on a material that has a small thermal mass and that is a poor heat conductor (such as a small $LiNbO_3$ plate). At shorter wavelengths, such as 633 nm, reflectance from the gold-black coating is diffuse and small.[14] From 2.5 to 10 μm, the reflectance gradually becomes more nearly specular and gradually increases to as much as 15%.

The absorptance of the gold-black coating determines the relative spectral responsivity, provided that the transmission through the detector is negligible and the reflectance is low. Then the relative spectral response of the detector can be determined from a spectral-reflectance measurement, if we assume that the gold-black transmittance is negligible and the relative detector response is proportional to 1 minus the measured reflectance.

The spectral reflectance was compared with a white polytetraflouroethylene (PTFE) reflectance standard. An oval beam, oriented at a 6° angle of incidence over the wavelength range 0.8 and 1.8 μm, made an 8 mm × 6 mm image at the detector. The 10-mm-diameter aperture of the detector was removed to avoid baffling. A 20-cm-diameter integrating sphere collected the diffuse radiation reflected back from the detector surface.

The measured signal from radiation reflected from the white-PTFE standard was used as the value for the 100% reflectance. Zero reflectance was recorded with a light trap, which replaced the detector at the sample port of the sphere. Ten wavelength scans were made in each measurement mode to improve the poor signal-to-noise ratio. The diffuse spectral reflectance of the detector was calculated from the averages of the ten measured reflectance values. The reflectance ρ at wavelength λ was calculated with

$$\rho(\lambda) = \frac{A_d(\lambda) - A_t(\lambda)}{A_s(\lambda) - A_t(\lambda)}. \tag{4}$$

In this expression, $A_s(\lambda)$ is the average signal of the white standard spectral-reflectance measurements, $A_d(\lambda)$ is the average signal of the detector spectral-reflectance measurements, and $A_t(\lambda)$ is the average signal of the light trap spectral-reflectance measurements.

Figure 14 shows the average reflectance, and standard uncertainty versus wavelength. We improved the signal-to-noise ratio of approximately 5:1 of the reflectance measurements by a factor of nearly 2 by averaging the measurement results of five neighboring wavelengths. A second-order polynomial fit to the calculated reflectance. The figure shows a spectral reflectance of 0.5–0.7% between 0.8 and 1.8 μm. This corresponds to a detector response change of 0.2% in this spectral range. Overall, the absolute reflectance from the gold black was low (less than 1%).

The angular response change of the detector was first measured in power measurement mode in which the detector aperture was underfilled by a 3-mm-diameter, He–Ne (633-nm) laser beam. Thereafter,

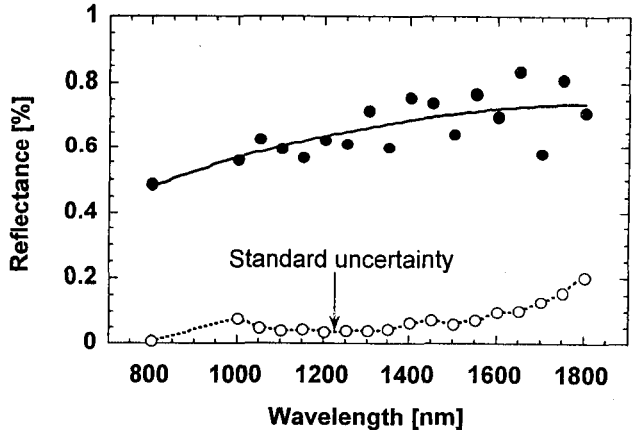

Fig. 14. Domain-engineered pyroelectric detector total reflectance and measurement standard uncertainty versus wavelength. Solid curve, polynomial fit to the averaged reflectance data.

the angular response was measured in irradiance mode in which the detector aperture was overfilled with a halogen lamp beam. For both measurement modes the aperture was circular and 8 mm in diameter. Figure 15 shows the optical arrangement for these tests. The detector was positioned a distance, D, 0.9 m from the laser and 0.55 m from the halogen lamp. The detector reflectance was then evaluated by rotation of the detector, incremental values of angle ϵ, relative to the optical axis, up and down (ϕ = 90°, $\epsilon = \pm 40°$), and side to side (ϕ = 0°, $\epsilon = \pm 40°$).

The directional error in underfilled mode was calculated as

$$f_2'(\epsilon, \phi) = \frac{E_r(\epsilon, \phi)}{E_r(\epsilon = 0°)} - 1, \tag{5}$$

where $E_r(\epsilon, \phi)$ and $E_r(\epsilon = 0°)$ were the detector readings for the incident radiation, E, arriving at incidence angles of ϵ and 0°. This definition is similar to the Commission Internationale de l'Eclairage (CIE) recommended directional error f_2 (ϵ, ϕ).[14]

Figure 16 shows the directional error, $f_2'(\epsilon)$, at a detector orientation of ϕ = 90°. The results of the horizontal (ϕ = 90°) and the vertical (ϕ = 0°) scans were very similar to each other. The response change was less than the measurement uncertainty in the range $\epsilon = \pm 11°$ and increased to ~0.1% at ϵ =

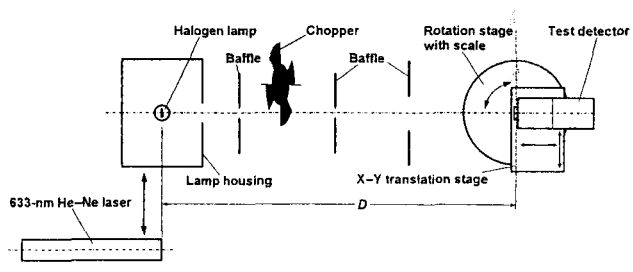

Fig. 15. Arrangement of the angular response measurements. The laser is used in underfilled mode, and the lamp is used in overfilled mode.

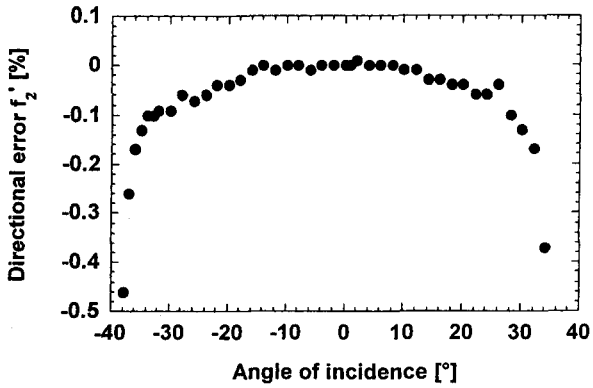

Fig. 16. Directional (relative angular) error of the pyroelectric detector in the vertical plane versus incidence angle. The incident laser radiation underfilled the detector aperture.

$\pm 30°$. The relative uncertainty ($k = 1$) of the directional error determinations was 0.04%.

The directional error in the overfilled-measurement mode was calculated according to the CIE recommendation, with the expression

$$f_2(\epsilon, \phi) = \frac{E_r(\epsilon, \phi)}{E_r(\epsilon = 0°)\cos \epsilon} - 1, \qquad (6)$$

where the denominator is the cosine response of an ideal detector-irradiance measurement.[15]

The measurement results of the horizontal-detector scan are shown in Fig. 17. According to the graph the angular response of the pyroelectric irradiance meter follows the cosine function, with a directional error of less than 0.1% within a $f/2$ field of view (31° full angle). The $\epsilon = 2°$ angular offset was caused by the asymmetric detector alignment on the rotation stage. The relative uncertainty of the directional error determinations in the irradiance measurement mode was 0.06% (coverage factor $k = 1$).

Comparison of the available detector candidates for infrared radiometric applications would constitute a paper in itself, but there are several key performance issues on which we can focus to abbreviate our discussion. In general, the uncertainty in radiometric measurements is reduced when detector variables such as response linearity, spatial and spectral uniformity, and temperature dependence are well characterized or known to be invariable.

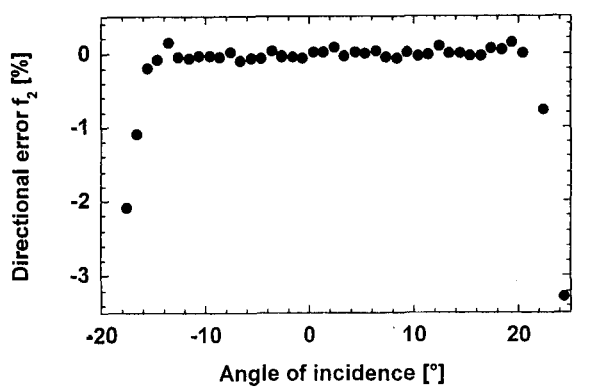

Fig. 17. Directional (relative angular) error of the pyroelectric detector in the horizontal plane versus incidence angle. The incident lamp radiation overfilled the detector aperture.

Table 1. Summary of Radiometer Properties

Property	Value
Power response at 633 nm	1.05×10^{-7} A/W
Temperature coefficient between 24 and 40 °C	0.15%/°C
Dark NEP	32 nW/Hz$^{1/2}$
NEP in the 1-nW–100-μW input radiant power range	38 nW/Hz$^{1/2}$
3-dB point with the OPA111 I-V converter in the 10^8-V/A range	570 Hz
3-dB point with the OPA111 I-V converter in the 10^9-V/A range	60.5 Hz
Spatial response nonuniformity within a 7.5-mm-diameter (633-nm, 0.5 mm-diameter) probe beam	±0.1%
Angular error in underfilled mode for $\epsilon \leq 30°$ incident angles	$f_2(\epsilon) < 0.1\%$
Angular error with 8-mm overfilled aperture for $\epsilon \leq 15°$	CIE $f_2(\epsilon) < 0.1\%$
Spectral reflectance variation (800–1800 nm)	<0.2%

The biggest drawbacks to using a pyroelectric detector are low optical sensitivity, high acoustic sensitivity, and the need to use an optical chopper. However, pyroelectric detectors can be operated at room temperature, and the chopper and the necessary electronics are not much more cumbersome than what is necessary for the competing alternatives. Photoconductors, such as mercury cadmium telluride (HgCdTe) and indium antimonide (InSb), have high sensitivity and are commonly used for transfer standards, but large-area (3–5-mm-diameter) devices are not highly uniform spatially and spectrally. The best photoconductors of this type have spatial nonuniformity variations as great as 3% and commonly to as great as 20% or more.[16] On this basis alone a pyroelectric detector with nearly four times the area (compared with the competing alternatives) and with 0.1% spatial-response variation is an excellent choice. In addition, we have demonstrated that domain-engineering techniques can reduce the acoustic sensitivity and give us confidence that the NEP is constant and linear at low power.

A summary of the properties of the domain-engineered pyroelectric radiometer is given in Table 1. Future improvements will be directed at reducing the temperature dependence and optimizing the domain-engineered areas and pattern, to further reduce the acoustic sensitivity. Further evaluation will include spectral responsivity and reflectance measurements at longer infrared wavelengths between 2 and 20 μm.

5. Conclusions

We have successfully used domain engineering to build a practical and convenient pyroelectric radi-

ometer with low acoustic sensitivity and high spatial and spectral response uniformity. We have demonstrated that a properly designed, applied, and characterized pyroelectric radiometer is well suited as a high-accuracy transfer standard for optical power and irradiance measurements. The domain-engineered pyroelectric radiometer is the only alternative compared with HgCdTe, InSb photoconductors, or commercially available pyroelectric detectors, capable of measurement uncertainty of the order of 0.1%. The primary role of the radiometer will be to extend and improve the National Institute of Standards and Technology spectral-responsivity scale from the visible to the near-infrared wavelength range.

References

1. J. H. Lehman and J. A. Aust, "Bicell pyroelectric optical detector made from a single $LiNbO_3$ domain-reversed electret," Appl. Opt. **37,** 4210–4212 (1998).
2. W. R. Blevin and W. J. Brown, "Black coatings for absolute radiometers," Metrologia **2,** 139–143 (1996).
3. L. Harris, R. McGinnies, and B. M. Siegel, "The preparation and optical properties of gold blacks, "J. Opt. Soc. Am. **38,** 582–589 (1948).
4. E. L. Dereniak and D. G. Crowe, *Optical Radiation Detectors* (Wiley, New York, 1984), p. 177.
5. G. Eppeldauer, "Temperature monitored/controlled silicon photodiodes for standardization," in *Advanced Fiber Communications Technologies*, L. G. Kazovsky, ed., Commission Internationale de l'Éclairage, Proc. SPIE **1479,** 71–77 (1991).
6. G. Eppeldauer, "Chopped radiation measurements with large area Si photodiodes," J. Res. Natl. Inst. Stand. Technol. **103,** 153–162 (1998).
7. A. L. Migdall and G. P. Eppeldauer, *Spectroradiometric Detector Measurements: III. Infrared Detectors*, Natl. Inst. Stand. Technol. Spec. Publ. 250–42 (National Institute of Standards and Technology Measurement Services, Gaithersburg, Md., 1998).
8. L. Lyons, *A Practical Guide to Data Analysis for Physical Science Students* (Cambridge U. Press, Cambridge, UK, 1991), p. 15.
9. T. C. Larason, S. S. Bruce, and A. C. Parr, *Spectroradiometric Detector Measurements: I. Ultraviolet Detectors and II. Visible to Near-Infrared Detectors*, Natl. Inst. Stand. Technol. Spec. Publ. 250–41 (National Institute of Standards and Technology Measurement Services, Gaithersburg, Md., 1998).
10. N. E. Byer, S. E. Stokowski, and J. D. Venables, "Complementary domain pyroelectric detectors with reduced sensitivity to mechanical vibrations and temperature changes," Appl. Phys. Lett. **27,** 639–641 (1975).
11. S. B. Lang, *Sourcebook of Pyroelectricity* (Gordon & Breach, New York, 1974), 40–48.
12. W. L. Wolfe and G. J. Zissis, *The Infrared Handbook* (Environmental Research Institute of Michigan, Ann Arbor, Mich., 1989), p. 7–79.
13. D. J. Advena, V. T. Bly, and J. T. Cox, "Deposition and characterization of far-infrared absorbing gold black films," Appl. Opt. **32,** 1136–1144 (1993).
14. G. W. Day, C. A. Hamilton, and K. W. Pyatt, "Spectral reference detector for the visible to 12-μm region; convenient, spectrally flat," Appl. Opt. **15,** 1865–1868 (1976).
15. Central Bureau of the Commission Internationale de L'Éclairage, *Methods of Characterizing the Performance of Radiometers and Photometers*, CIE Publications, 53 (TC-2.2) (Central Bureau of the Commission Internationale de L'Éclairage, Vienna, Austria, 1982).
16. E. Theocharous, N. P. Fox, and T. R. Prior, "A comparison of the performance of infrared detectors for radiometric applications, in *Optical Radiation Measurements III*, J. M. Palmer, ed., Proc. SPIE **2815,** 56–68 (1996).